



AFRL-RY-WP-TR-2014-0216

**PARTICLE-BASED SIMULATIONS OF MICROSCOPIC
THERMAL PROPERTIES OF CONFINED SYSTEMS**

Flavio Sabatti, Ky Merrill, Stephen Goodnick, and Marco Saraniti
Arizona State University

NOVEMBER 2014
Final Report

Approved for public release; distribution unlimited.
See additional restrictions described on inside pages

STINFO COPY

**AIR FORCE RESEARCH LABORATORY
SENSORS DIRECTORATE
WRIGHT-PATTERSON AIR FORCE BASE, OH 45433-7320
AIR FORCE MATERIEL COMMAND
UNITED STATES AIR FORCE**

NOTICE AND SIGNATURE PAGE

Using Government drawings, specifications, or other data included in this document for any purpose other than Government procurement does not in any way obligate the U.S. Government. The fact that the Government formulated or supplied the drawings, specifications, or other data does not license the holder or any other person or corporation; or convey any rights or permission to manufacture, use, or sell any patented invention that may relate to them.

This report is the result of contracted fundamental research deemed exempt from public affairs security and policy review in accordance with SAF/AQR memorandum dated 10 Dec 08 and AFRL/CA policy clarification memorandum dated 16 Jan 09. This report is available to the general public, including foreign nationals.

AFRL-RY-WP-TR-2014-0216 HAS BEEN REVIEWED AND IS APPROVED FOR PUBLICATION IN ACCORDANCE WITH ASSIGNED DISTRIBUTION STATEMENT.

*//Signature//

JOHN D. BLEVINS, Program Manager
Devices for Sensing Branch
Aerospace Components & Subsystems Division

*//Signature//

ROSS W. DETTMER, Chief
Devices for Sensing Branch
Aerospace Components & Subsystems Division

*//Signature//

JACQUELINE S. JANNING-LASK, Chief
Aerospace Components & Subsystems Division
Sensors Directorate

This report is published in the interest of scientific and technical information exchange, and its publication does not constitute the Government's approval or disapproval of its ideas or findings.

*Disseminated copies will show “//signature//” stamped or typed above the signature blocks.

REPORT DOCUMENTATION PAGE					Form Approved OMB No. 0704-0188	
<p>The public reporting burden for this collection of information is estimated to average 1 hour per response, including the time for reviewing instructions, searching existing data sources, searching existing data sources, gathering and maintaining the data needed, and completing and reviewing the collection of information. Send comments regarding this burden estimate or any other aspect of this collection of information, including suggestions for reducing this burden, to Department of Defense, Washington Headquarters Services, Directorate for Information Operations and Reports (0704-0188), 1215 Jefferson Davis Highway, Suite 1204, Arlington, VA 22202-4302. Respondents should be aware that notwithstanding any other provision of law, no person shall be subject to any penalty for failing to comply with a collection of information if it does not display a currently valid OMB control number. PLEASE DO NOT RETURN YOUR FORM TO THE ABOVE ADDRESS.</p>						
1. REPORT DATE (DD-MM-YY) November 2014		2. REPORT TYPE Final		3. DATES COVERED (From - To) 7 June 2010 – 30 July 2014		
4. TITLE AND SUBTITLE PARTICLE-BASED SIMULATIONS OF MICROSCOPIC THERMAL PROPERTIES OF CONFINED SYSTEMS				5a. CONTRACT NUMBER FA8650-10-1-7045		
				5b. GRANT NUMBER		
				5c. PROGRAM ELEMENT NUMBER 62716E		
6. AUTHOR(S) Flavio Sabatti, Ky Merrill, Stephen Goodnick, and Marco Saraniti				5d. PROJECT NUMBER DARPA		
				5e. TASK NUMBER YD		
				5f. WORK UNIT NUMBER Y0GC		
7. PERFORMING ORGANIZATION NAME(S) AND ADDRESS(ES) Arizona State University P.O. Box 876011 Tempe, AZ 85287-6011				8. PERFORMING ORGANIZATION REPORT NUMBER		
9. SPONSORING/MONITORING AGENCY NAME(S) AND ADDRESS(ES) Air Force Research Laboratory Sensors Directorate Wright-Patterson Air Force Base, OH 45433-7320 Air Force Materiel Command United States Air Force				10. SPONSORING/MONITORING AGENCY ACRONYM(S) AFRL/Rydd		
				11. SPONSORING/MONITORING AGENCY REPORT NUMBER(S) AFRL-RY-WP-TR-2014-0216		
12. DISTRIBUTION/AVAILABILITY STATEMENT Approved for public release; distribution unlimited						
13. SUPPLEMENTARY NOTES This report is the result of contracted fundamental research deemed exempt from public affairs security and policy review in accordance with SAF/AQR memorandum dated 10 Dec 08 and AFRL/CA policy clarification memorandum dated 16 Jan 09. Report contains color						
14. ABSTRACT We discuss in this report the final results of a research program whose goal was the development of a modeling approach for the thermal management of solid-state devices at the microscopic level. By the inclusion of the phonon dynamics within the framework of charge transport, we implemented extremely efficient microscopic models in CAD tools for the design of electron devices where the generation and the transport of thermal energy are functionally coupled with their electrical specifications.						
15. SUBJECT TERMS particle-based simulation, electron devices, cellular monte carlo, full band, phonons						
16. SECURITY CLASSIFICATION OF:			17. LIMITATION OF ABSTRACT: SAR	18. NUMBER OF PAGES 26	19a. NAME OF RESPONSIBLE PERSON (Monitor) John Blevins	
a. REPORT Unclassified	b. ABSTRACT Unclassified	c. THIS PAGE Unclassified			19b. TELEPHONE NUMBER (Include Area Code) N/A	

Table of Contents

Section	Page
List of Figures	ii
List of Tables	ii
1.0 Summary	1
2.0 Introduction.....	2
3.0 Methods, Assumptions, and Procedures	3
3.1 Rejection Algorithm for Scattering	3
3.2 Phonon-Phonon Scattering Rate.....	4
3.3 Phonons Initialization and Boundary Conditions.....	4
4.0 Results and Discussion	6
4.1 Validation of the Phonon Scattering Rate	6
4.2 Phonon-Isotope Scattering	7
4.3 Phonon Dynamics	8
4.4 Phonon-Electron Interaction	9
4.5 Beyond the Heat Equation: Energy Balance Equation Solver	11
4.6 Boundary Conditions.....	14
5.0 Conclusions.....	18
6.0 References.....	19
List of Symbols, Abbreviations, and Acronyms	20

List of Figures

Figure	Page
Figure 1: Flow Chart of the Rejection Algorithm.....	3
Figure 2: Simulated Evolution of a System Initialized with a Non-equilibrium Distribution of Phonons	6
Figure 3: Simulated and Experimentally Determined Effects of Phonon-Isotope Scattering on Low Temperature Thermal Conductivity: the Natural Silicon <i>Sinat</i>	8
Figure 4: Comparison between the Theoretical Temperature Distribution (dashed lines), and the Monte Carlo Simulation (solid lines)	9
Figure 5: Validation of the Rejection Algorithm by Simulation of the GaAs Electron Drift Velocity versus Electric Field	10
Figure 6: Electron Drift Velocity versus Electric Field in Silicon at Different Temperature.....	11
Figure 7: Steady-State Temperature Distribution within a Device with the Left Contact set at 300K and the Right one at 310K	13
Figure 8: Results for the Dirichlet Boundary Condition.....	17
Figure 9: Results for the Robin Boundary Condition	17

List of Tables

Table	Page
Table 1. Main Milestones of the Project.....	2

1.0 Summary

In this document, we offer the final report of the Defense Advanced Research Projects Agency (DARPA)/United States Air Force (USAF) award # FA8650-10-1-7045. An overview of the project is discussed, and the progress of the research activity is assessed, as related to the program milestones.

2.0 Introduction

Within this project, a novel modeling approach is being defined for the development of a transformational technology based on the microscopic thermal management of solid-state devices. By the full inclusion of the phonon dynamics within the framework of charge transport, we are implementing microscopic models in our existing particle-based Cellular Monte Carlo (CMC) computer-aided design (CAD) tools [1] for the design of electron devices where the generation and the transport of thermal energy are functionally coupled with their electrical specifications. The crucial challenges of the present phase of the project are summarized in the following three tasks:

1. Implementation of a rejection algorithm for the electron-phonon scattering table.
2. Realization of a solver for the heat transport equation.
3. Integration of phonons and electrons in a unified particle-based framework.

Table 1. Main Milestones of the Project

Task	Milestone	Deliverable	Months after award (MAA)
1	Code design, derivation of temperature –dependent phonon rates		2 MAA
1	Implementation of rejection in electron-phonon scattering	Report describing new algorithms	4 MAA
2	Implementation of a solver for the heat transport equation.	Study of thermal conductivity in simple 2D structure	5 MAA
3	Integration of phonons and electrons in a unified particle-based framework.	Report	6 MAA

Accordingly to the statement of work, such tasks have been organized in the following milestones:

This is the final report that summarizes the methodology developed to model phonon-phonon and phonon-electron interaction within a perturbative full-band approach.

3.0 Methods, Assumptions, and Procedures

3.1 Rejection Algorithm for Scattering

The capabilities of the original CMC algorithm [1] have been extended using a rejection algorithm. This approach retains the simulation speed advantages of the CMC scheme while allowing the adaptation of the scattering rates to the real time local conditions. Figure 1 shows the rejection algorithm flow chart. After the CMC triggers an event with probability P_{CMC} , a new scattering probability P_{loc} is computed from the local conditions. The rejection probability $P_{rej}=P_{loc}/P_{CMC}$ is then used in a stochastic procedure to decide whether the scattering event occurs or is rejected.

The scattering probability after the rejection is

$$P_{q \rightarrow q'} = P_{CMC} * \left(\frac{P_{loc}}{P_{CMC}} \right) = P_{loc} \quad (1)$$

where q is the initial state, and q' the final state.

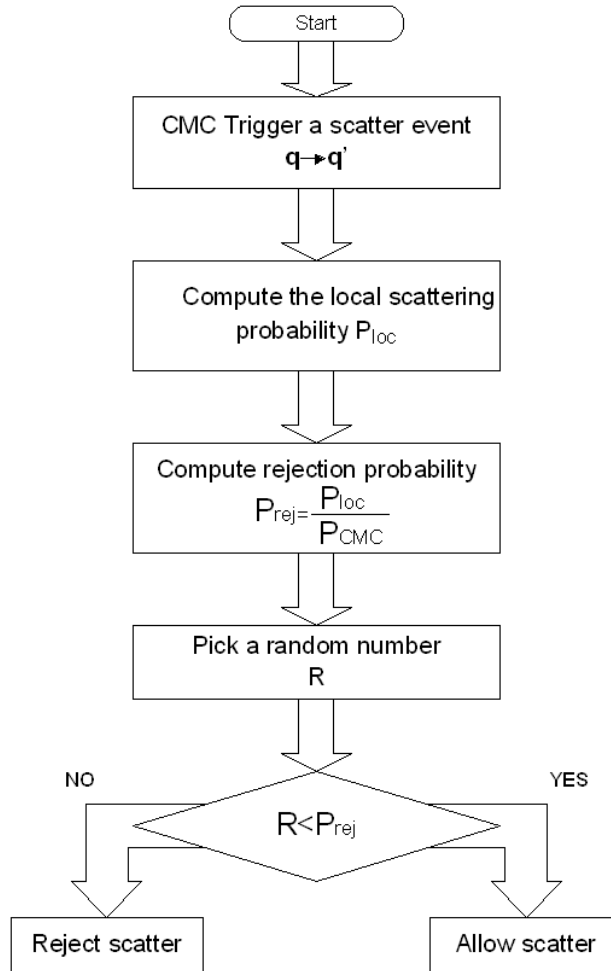


Figure 1: Flow Chart of the Rejection Algorithm

3.2 Phonon-Phonon Scattering Rate

Perturbation theory is used to implement both phonon-phonon and phonon-defect interactions. The anharmonic decay and recombination scattering rate based on the Klemens model [2] is given by the following expression:

$$P_{q \rightarrow q', q''} = \frac{2\hbar}{M^3} \frac{c^2(\mathbf{q}, \mathbf{q}', \mathbf{q}'')}{\omega \omega' \omega''} \delta(\omega, \omega', \omega'') \delta(\mathbf{q}, \mathbf{q}', \mathbf{q}'') F_{loc} \quad (2)$$

where $F_{loc} = F(n'_{loc}, n''_{loc})$ is a local population dependent factor, n'_{loc} and n''_{loc} are the populations at \mathbf{q}' and \mathbf{q}'' , respectively, M is the average mass, $c^2(\mathbf{q}, \mathbf{q}', \mathbf{q}'')$ is the anharmonic coefficient obtained from the perturbation Hamiltonian, and ω, ω' and ω'' are the angular frequencies corresponding to the states \mathbf{q}, \mathbf{q}' , and \mathbf{q}'' , respectively.

The phonon-defect scattering probability based on the work of Srivastava [3] is given by:

$$P_{q \rightarrow q'} = \frac{V_w \Gamma}{6} \omega \omega' (\mathbf{e}_q^* \cdot \mathbf{e}_{q'})^2 \delta(\omega - \omega') (n'_{loc} + 1) \quad (3)$$

where \mathbf{e} is the polarization vector, V_w is the Wigner-Seitz cell volume, and Γ is an expression that depends on the phonon-defect type to be discussed later.

Computing the local scattering probability requires estimating the local phonon populations n'_{loc} and n''_{loc} from the ensemble. This task requires defining a sampling volume of the particle position both in real space (V_{loc}) and in momentum space (Ω_{loc}), then counting the number of simulated phonons $\eta(\Omega_{loc}, V_{loc})$ in the volume, and, finally, obtaining the phonon population using the following approximation:

$$n_{loc} \cong \frac{\eta(\Omega_{loc}, V_{loc})}{N_{state}} = \eta(\Omega_{loc}, V_{loc}) * \frac{8\pi^3}{\Omega_{loc} V_{loc}} \quad (4)$$

where N_{state} is the number of states in the volume.

3.3 Phonons Initialization and Boundary Conditions

The number of equilibrium phonons within a sampling volume V_{loc} in a crystal of volume V_c is:

$$N_{pho}(T, V_{loc}) = \frac{V_{loc}}{V_c} \sum_p \sum_q \langle n_{q,p}, T \rangle \quad (5)$$

where p is the phonon mode index, $\langle n_{q,p}, T \rangle$ is the Bose-Einstein distribution, and T is the temperature. Typically, $N_{pho}(T, V_{loc})$ is an extremely large number, and even within the relatively small volume of a modern transistor there are too many particles to simulate individual phonons practically. For this reason, a weighting factor W is used, and each simulated particle represents W real particles. The factor W is computed before starting the simulation using the formula:

$$W = \frac{N_{dev}}{N_{sim}}, \quad (6)$$

where N_{dev} is the total number of real phonons in the device and N_{sim} the number of super particles to be simulated.

The particle-based phonon Monte Carlo code implements three boundary conditions: (1) planar interfaces, (2) rough interfaces, and (3) contacts. The first boundary condition models ideal surfaces, in which the incident particle is specularly reflected. The second boundary condition models interfaces between the extreme cases of perfectly specular reflection, considered above and perfectly diffuse reflection. The model is based on the work of Fuchs-Sondheimer [4] [5] and adapted to the full band approach. Contacts are modeled as ideal reservoirs with infinite thermal capacity and constant temperature. The contact population is replenished injecting phonons in the reservoir using a velocity-weighted probability distribution, similar to Pardo [6].

4.0 Results and Discussion

4.1 Validation of the Phonon Scattering Rate

Tests have been designed to verify the algorithm's capability of adapting to the real-time local particle distribution. The first test verifies the capability of the scattering algorithm to reach the equilibrium steady state distribution, while a second test verifies the capability of reproducing experimentally observed results over a wide range of temperatures.

Let's consider an adiabatic system with total energy density E_c . For any initial energy distribution, the phonons will eventually reach a Bose-Einstein distribution with temperature T_c ($\langle n_{q,p}, T_c \rangle$) that satisfies the following energy vs. temperature relationship:

$$E_c(T_c) = \frac{1}{V_c} \sum_p \sum_q \left(\langle n_{q,p}, T_c \rangle + \frac{1}{2} \right) \hbar \omega_q \quad (7)$$

Figure 2 shows the energy distribution at the initial and the final state of the simulation. The system is initialized with energy density corresponding to a temperature of 200 Kelvin (K), $E_c(200K)$, but the initial distribution is set as that corresponding to a temperature of 300K, $d_{ini}(\mathbf{q}, p) \propto \langle n_{q,p}, 300 \rangle$ (red line). The system is allowed to evolve until it reaches steady state (black line), at which time the energy density corresponding to the theoretical distribution $\langle n_{q,p}, 200K \rangle$ (blue line) is obtained.

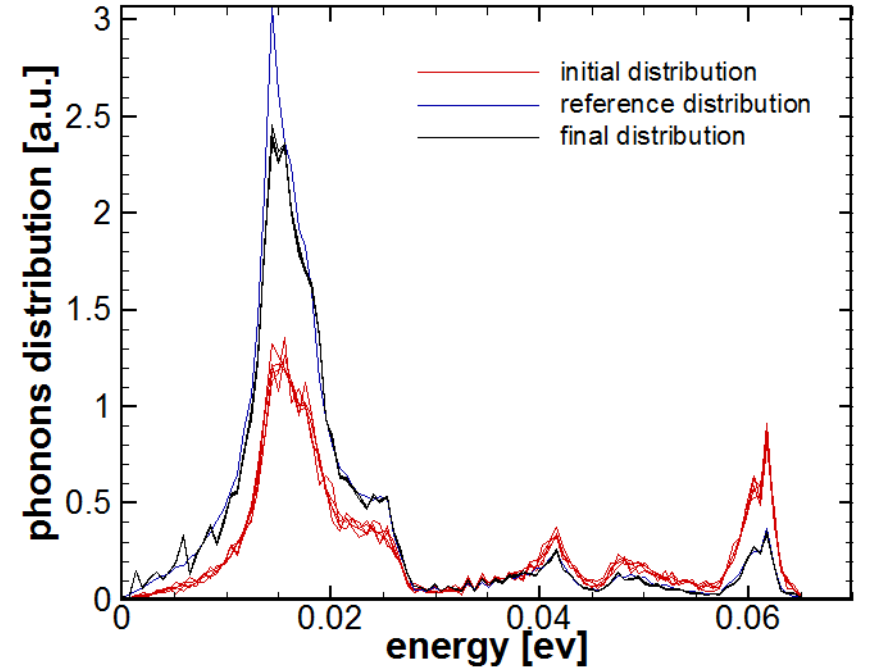


Figure 2: Simulated Evolution of a System Initialized with a Non-equilibrium Distribution of Phonons

The system evolves to a final distribution coincident to the analytical reference distribution.

4.2 Phonon-Isotope Scattering

An isotope is an atomic variant of an element with the nominal number of protons, but a different number of neutrons and hence a different atomic mass. For example, C^{12} , C^{13} , and C^{14} are isotopes of Carbon having 12, 13, and 14 neutrons, respectively. The isotopes of an element show identical chemical behavior (except in the reaction speed) as well as both crystal and electronic structure, however, the difference in mass disrupts the periodicity of the crystal resulting in a large phonon scattering rate. The overall effect of this is seen in a large reduction of the thermal conductivity tensor (\mathbf{k}).

The thermal conductivity of the natural crystal (\mathbf{k}_{nat}) and the isotopically pure crystal (\mathbf{k}_{iso}) can differ by up to one order of magnitude at low temperatures [7]. At room temperature the effect is more ambiguous, and even for a material studied as extensively as silicon (Si) the reported k_{iso} range is between 110% [8] [9] and 160% [10] [11] [12] of the k_{nat} value. For these reasons isotope scattering cannot be overlooked in the simulation of real semiconductor across different ranges of temperature. Isotope scattering is implemented as a phonon-defect scatter; using Srivastava's model expressed in equation (3) where the parameter Γ is given by:

$$\Gamma = \sum_i f_i \left(\frac{\Delta M_i}{\bar{M}} \right) \quad (8)$$

and where f_i is the fraction of atom with mass M_i , and \bar{M} the average mass.

Figure 3 shows the effect on the thermal conductivity of Si of the scattering model implemented in our particle based code. The lines represent the measured [8] thermal conductivity of natural silicon Si^{nat} (92.2% Si^{28} , 4.6% Si^{29} 3.1% Si^{32}) and an isotopically enriched sample of Si^{28} . The simulations without the isotope scattering follow the isotopically pure thermal conductivity, while including the isotope scattering model allows for accurate reproduction of the Si^{nat} thermal conductivity.

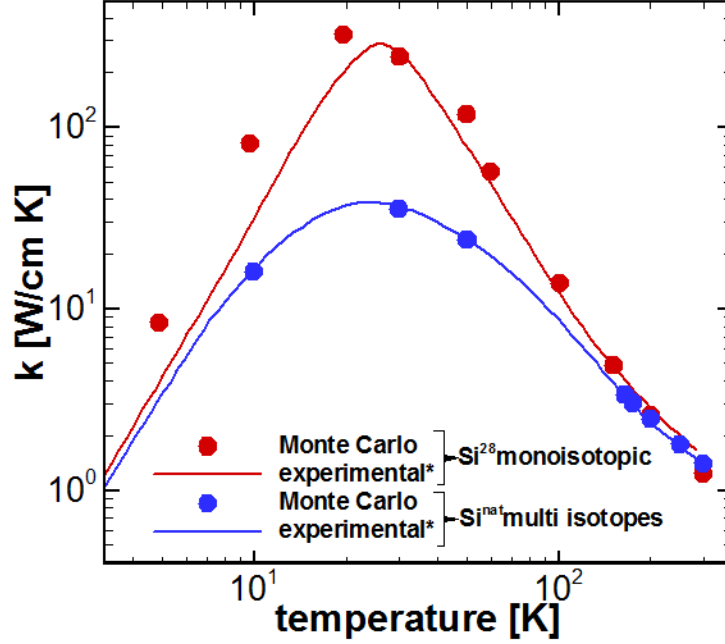


Figure 3: Simulated and Experimentally Determined Effects of Phonon-Isotope Scattering on Low Temperature Thermal Conductivity: the Natural Silicon Si^{nat}
92.2% Si^{28} , 4.6% Si^{29} 3.1% Si^{32} is compared to the Si^{28} enriched sample. The agreement is excellent

4.3 Phonon Dynamics

The ability of the Monte Carlo approach to reproduce thermal transients has been tested on a thermal resistor with a length of 2 micrometers. The device has two lateral contacts set to temperatures $T_H = 310K$ and $T_L = 290K$, and the device is initialized at the temperature T_L . During the simulation, the transient effective temperature is extracted from the local energy density by inverting the energy vs. temperature relationship seen previously in equation (7).

The simulated evolution of the temperature can be estimated analytically by solving Fick's law of diffusion. An approximate analytical solution of Fick's law may be obtained by means of the Laplace transform:

$$T_F(x, t) = T_L + (T_H - T_L) \left[\operatorname{erfc} \left(\frac{x}{2\sqrt{tD}} \right) - \operatorname{erfc} \left(\frac{2L - x}{2\sqrt{tD}} \right) + \operatorname{erfc} \left(\frac{2L + x}{2\sqrt{tD}} \right) \right] \quad (9)$$

where T_F is the estimated temperature, t the time, D the diffusion coefficient, L the length of the device, and erfc is the complementary error function. The complementary error function erfc is related to the error function by $\operatorname{erfc}(z) = 1 - \operatorname{erf}(z)$, and the error function itself is defined as:

$$\operatorname{erf}(z) = \frac{2}{\sqrt{\pi}} \int_0^z e^{-t^2} dt \quad (10)$$

Figure 4 shows both the theoretical temperature distribution (dashed lines) and the results of Monte Carlo simulation (solid lines) being averaged over 50 simulations (each one with different random number seed). The full band phonon Monte Carlo is seen to follow the estimation from Fick's law at each time.

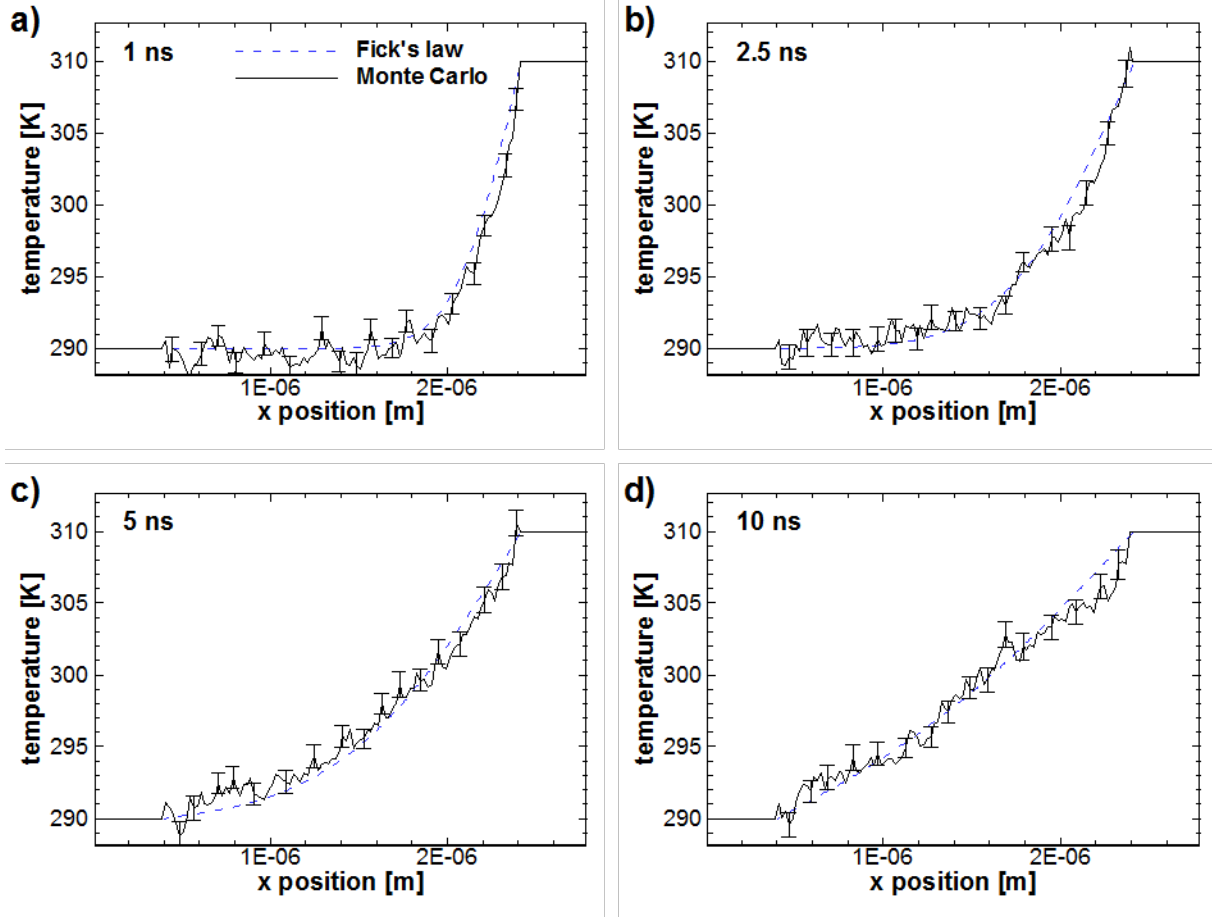


Figure 4: Comparison between the Theoretical Temperature Distribution (dashed lines), and the Monte Carlo Simulation (solid lines)

The simulations follow the analytical solution during the time transient.

4.4 Phonon-Electron Interaction

Within the CMC framework the scattering probabilities from all initial states to all the possible final states are pre-computed for a specific temperature and stored in a lookup scattering table. Whenever a scattering event occurs, the final state is chosen from the lookup table. This approach would require using a different scattering table to model different temperatures. A new structure for the scattering table and an enhanced scattering algorithm has been designed to model a wide range of temperatures using only one table while retaining the speed advantage of the CMC.

The new structure uses a two level approach. Each element of the first level array contains the information used in a typical Ensemble Monte-Carlo (EMC), e.g., the scattering rate, scattering mechanism, phonon mode involved, etc. Each element of the EMC array is linked to a second

array (CMC array), which contains all the possible final states and the scattering probability for that mechanism. The new algorithm requires two steps: first the new scattering table is pre-computed according to an expected maximum temperature (T_{max}), second a rejection technique is used to adapt the scattering probability to the local temperature (T_{loc}).

Based on this scheme, the scattering is modeled as a five step process:

1. The scattering table is pre-computed for the maximum expected temperature T_{max} .
2. A scattering mechanism is chosen from the EMC array
3. A final state is chosen from the related CA array
4. A rejection probability is computed according to the local runtime conditions
5. A stochastic process establishes whether the scattering occurs or is rejected.

Figure 5 shows the electron drift velocity versus electric field in gallium arsenide (GaAs) computed with the original CMC table structure (squares) at temperature $T=150K$, and the new structure with the rejection technique (solid lines) with $T_{max}=400K$ and $T_{loc}=150K$. The simulations overlap at low electric field, where the CMC grid is extremely fine. However, at high electric fields where the grid is coarser, the new structure produces a more accurate final state energy.

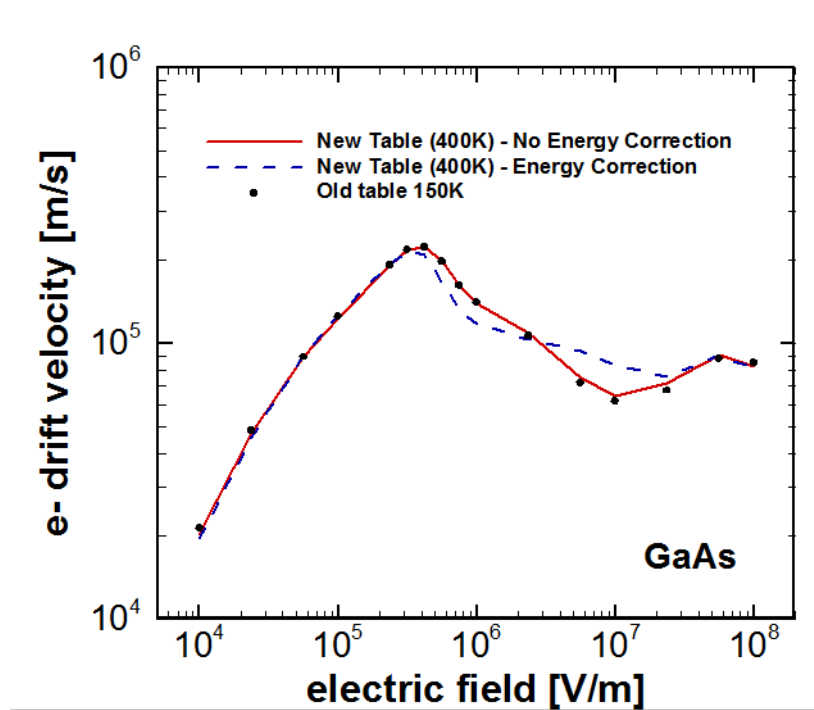


Figure 5: Validation of the Rejection Algorithm by Simulation of the GaAs Electron Drift Velocity versus Electric Field

The velocity computed using the rejection algorithm (red line) is identical to the one obtained with a fixed temperature table (dots). Further improvement is obtained by the implementation of the energy correction (dashed line)

Figure 6 shows the drift velocity versus electric field in Si at four different temperatures. The simulations employing the scattering table with the rejection technique (lines) are performed using the same pre-computed $T_{\max}=350\text{K}$ rejection table and varying T_{loc} , while the reference simulations (dots) use a separate table for each temperature.

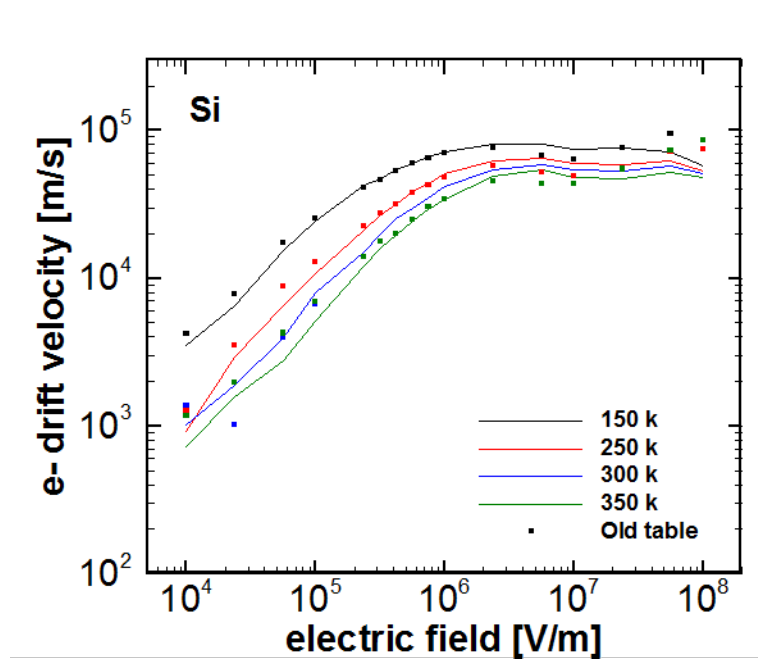


Figure 6: Electron Drift Velocity versus Electric Field in Silicon at Different Temperature
The lines are all computed using the same $T_{\max}=350\text{K}$ scattering table and the rejection technique, whereas the velocities represented by dots are computed using fixed temperature tables

4.5 Beyond the Heat Equation: Energy Balance Equation Solver

The original research program proposed an efficient technique to reach thermal equilibrium within the device layout. This technique was based on a solution of the Heat Transport Equation (HTE) (flux-based) coupled self-consistently with the particle-based electron dynamics. Once the electro-thermal steady-state conditions were reached, the temperature map supplied by the HTE solver would have been replaced by a population of phonons and the particle-based phonon dynamics simulation engine would have been started in order to solve transients and non-equilibrium heat transport.

However, an approach based on solving the Energy Balance equation for phonons, in lieu of the Heat Transport Equation, was adopted. The Energy Balance approach is better suited to self-consistent coupling with the electron dynamics and allows a higher degree of accuracy by supplying a separate solution for each phonon mode (or group of modes). The approach developed here is based on the energy balance equation for each mode μ , directly obtained from the phonon Boltzmann Transport Equation (BTE):

$$\frac{\partial W_\mu}{\partial t} = -\nabla \cdot \mathbf{F}_W + \left. \frac{\partial W_\mu}{\partial t} \right|_{e-p} + \left. \frac{\partial W_\mu}{\partial t} \right|_{p-p} \quad (11)$$

where $W_\mu(\mathbf{r}, t) = \frac{1}{\Omega} \sum_{\mathbf{k}} E_\mu(\mathbf{k}) f_\mu(\mathbf{r}, \mathbf{k}, t)$ is the ensemble energy in the volume Ω of the reciprocal space, $\mathbf{F}_\mu(\mathbf{r}, t) = \frac{1}{\Omega} \sum_{\mathbf{k}} \mathbf{v}(\mathbf{k}) E_\mu(\mathbf{k}) f_\mu(\mathbf{r}, \mathbf{k}, t)$ is the energy flux, and the two partial derivatives of W_μ in the LHS of the equation represent the rate of change of the ensemble energy density due to electron-phonon and phonon-phonon interaction, respectively.

Under steady-state conditions the time derivative on the LHS must be zero, and hence the heat flux is given by the sum of electron-phonon and phonon-phonon contributions, i.e.,

$$\nabla \cdot (\kappa_\mu(T, \mathbf{r}) \nabla T) = - \left(\left. \frac{\partial W_\mu}{\partial t} \right|_{e-p} + \left. \frac{\partial W_\mu}{\partial t} \right|_{p-p} \right) = -P_\mu \quad (12)$$

where a Fourier Law approximation has been used for $\mathbf{F}_\mu(\mathbf{r}) = -\kappa_\mu(T, \mathbf{r}) \nabla T$, and the subscript μ denotes either the optical or acoustic phonon mode, respectively.

The CMC code includes efficient solvers for linear elliptical partial differential equations (PDEs), and thus it is desired to manipulate the energy balance equation in order to re-write it in the form of an elliptical PDE. The main issue with such manipulation is the dependency of κ_μ from the temperature and the position. We therefore assume that, with respect to the position, the thermal conductivity can be represented as a piece-wise function of the temperature, in other words, $\kappa_{\mu,C}(T)$ is a function of the temperature but is not changing with the position within each cell C of the finite differences grid. We therefore express this restricted position dependency with the index C rather than via a full functional dependence on the position vector \mathbf{r} .

With this in mind, we utilize the well-known Kirchhoff Transformation to define an ‘‘apparent’’ temperature $\theta_{\mu,C}(T)$:

$$\theta_{\mu,C}(T) = T_0 + \frac{1}{\kappa_{\mu,C}(T_0)} \int_{T_0}^T \kappa_{\mu,C}(\tau) d\tau \quad (13)$$

where T_0 is a reference temperature, and $\kappa_{\mu,C}(T_0)$ the thermal conductivity of the phonon mode μ at the reference temperature. This allows us to rewrite the energy balance equation as follows:

$$\nabla^2 \theta_{\mu,C} = - \frac{P_\mu(\mathbf{r})}{\kappa_{\mu,C}(T_0)} \quad (14)$$

which is a linear Poisson equation for the temperature $\theta_{\mu,C}(T)$. This final equation can be efficiently solved with the multi-grid solvers readily available in the code.

The temperature dependent thermal conductivity is available for many materials as a power law fit to experimental data [13]. Using these relationships, the Kirchhoff Transformation is computed within the code. This computation is performed for two groups of modes, the acoustic

and the optical, and it is assumed that the temperature dependence affects only the acoustic modes. The temperature value along with its corresponding acoustic and optical Kirchhoff temperatures are tabulated for each material at the beginning of a simulation and used for the Kirchhoff and inverse Kirchhoff transformations throughout the simulation.

To validate the approach, we have solved the above equation with the forcing function set to zero, i.e., within the diffusive regime. In this case we expect the solution to simply be linear in between two boundary “thermal contacts” where the temperature is specified. To verify our approach, a thermal GaAs resistor has been simulated where a right contact is initially set at 310K, while a left contact and all intermediate cells are set to 300K. The temperature map is first transformed into a Kirchhoff apparent temperature, then the PDE is solved, and finally the inverse transformation is applied to return to the “standard” temperature variable. The resulting temperature map is linear as expected as seen in Figure 7.

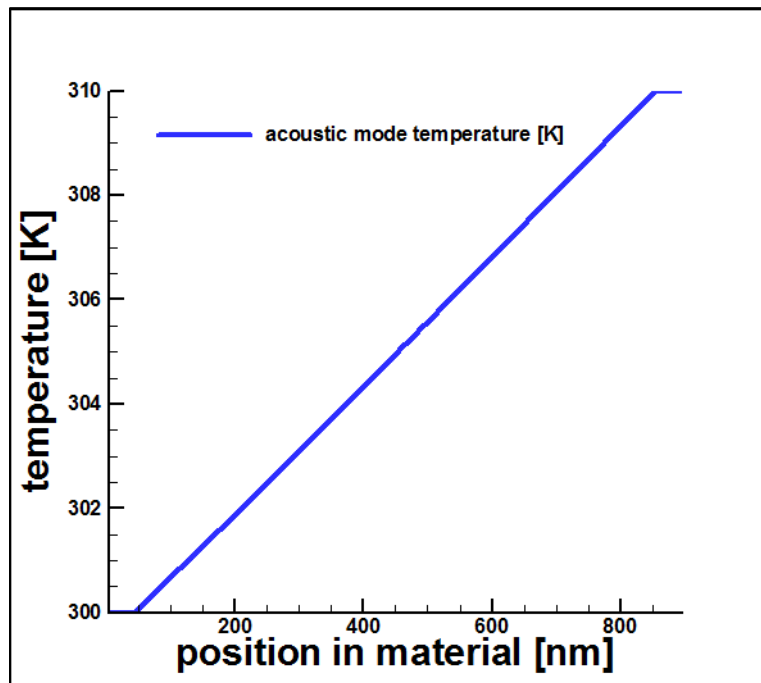


Figure 7: Steady-State Temperature Distribution within a Device with the Left Contact set at 300K and the Right one at 310K

The solution is linear in the region within the contacts as expected in the absence of a forcing function

Next, a manner to calculate the forcing function for the energy balance equation must be implemented. The forcing function for a phonon mode μ can be separated into individual contributions due to electron-phonon (e-p) scattering and to phonon-phonon (p-p) scattering, representing the rate of change of the phonon energy density for the particular mode, respectively. The forcing function P_μ is then written as:

$$-P_\mu = -\left(\frac{\partial W_\mu}{\partial t}\Big|_{e-p} + \frac{\partial W_\mu}{\partial t}\Big|_{p-p}\right) \quad (15)$$

The electron-phonon term in the forcing function can be computed by tracking the energy exchanged between phonons and electrons during scattering, while the phonon-phonon term is expressed using a relaxation time approximation [14]:

$$\frac{\partial W_\mu}{\partial t}\Big|_{op-ac} = -C_{op} \frac{T_{op} - T_{ac}}{\tau_{op-ac}}, \quad (16)$$

$$\frac{\partial W_\mu}{\partial t}\Big|_{ac-op} = -C_{ac} \frac{T_{ac} - T_{op}}{\tau_{ac-op}}, \quad (17)$$

where C_μ is the volumetric heat capacity $\left(\frac{J}{m^3K}\right)$, T_μ the temperature of mode μ , and τ_{i-j} the energy relaxation time between mode i and j . In the above equations, the subscripts *ac* and *op* denote the acoustic and optical modes, respectively.

4.6 Boundary Conditions

It was initially assumed that a simple Dirichlet boundary condition [15] [16] on a thermal contact would be sufficient for our simulation purposes. In the Dirichlet boundary condition, the temperature value is simply set on the boundaries where specified and not allowed to change from this prescribed value, i.e., $T_b = c$

However we observed that, both in the Monte Carlo simulations as well as the commercial simulator Synopsys [17], that this condition seemed to cool the system too much with peak temperatures in a biased device rising only a few Kelvin above room temperature. Other boundary conditions explored are those of the inhomogeneous Neumann [15] [16] and the Robin [15] [16] boundary conditions. It should be noted that the Robin boundary condition is also called a generalized Neumann condition within the Matlab [18] software PDE package. In addition, the Dirichlet boundary condition is sometimes called a boundary condition of the first kind, the Neumann boundary condition a boundary condition of the second kind, and the Robin boundary condition a boundary condition of the third kind [16].

The Neumann condition is that of prescribing the heat flux that leaves the specified boundary, and is expressed as:

$$\frac{\partial T}{\partial n} = f \quad (18)$$

while the related homogenous Neumann condition, for instance that of an insulating surface, is expressed as:

$$\frac{\partial T}{\partial n} = 0 \quad (19)$$

The problem with this condition is that it does not produce a unique solution, but rather a family of solutions differing by an additive constant of integration. Hence, to effectively use this condition the temperature must be prescribed at some location within the simulation domain R , i.e., there must be at least one point within the device in question at which we have a Dirichlet boundary condition. In addition the elliptic PDE with a Neumann boundary condition:

$$-\nabla^2 v = F \text{ in } R \quad (20)$$

$$\frac{\partial v}{\partial n} = g \text{ on } \partial R \quad (21)$$

is also subject to the following constraint [15]:

$$-\int_R F \, d(x, y) = \int_{\partial R} g \, dS. \quad (22)$$

The Robin boundary condition is expressed as

$$-k \frac{\partial T}{\partial n} = h(T - T_a) \quad (23)$$

where T is the interior temperature at the boundary and T_a is the temperature of the outside environment or, in our case, the temperature of the heat sink of the device. The heat transfer coefficient, h , has units $\frac{W}{m^2 K}$ and can be thought of as a thermal surface conductance, or the inverse of a thermal surface resistance. The role of the heat transport coefficient is to scale the outwardly directed flux based on how well heat should be dissipated away from the boundary. The Robin condition yields a unique solution as long as $\frac{k}{h} > 0$ [15].

The Dirichlet and Robin boundary conditions have been implemented and tested using a simple case with an analytic solution. In this test, a uniform piece of GaAs is used with either the Dirichlet or Robin condition set on the bottom plane of the material and a homogenous Neumann condition set on all other surfaces (meaning that zero heat flux leaves those surfaces).

The governing differential equation is a Poisson Equation of the form (in 1-D)

$$\frac{d^2T}{dy^2} = -\frac{q}{\kappa} , \quad (24)$$

which has a simple analytical solution of

$$T = -\frac{q}{2k}y^2 + C_1y + C_2 \quad (25)$$

The constant $C_1 = \frac{q*L}{k}$, where L is the length of the heat-generating material, for both the Dirichlet and Robin boundary conditions. For the Dirichlet condition, the constant C_2 is given by the temperature specified at the boundary, $C_2 = T_b$, while for the Robin condition it is found that $C_2 = T_a + \frac{q*L}{h}$.

Various values for the uniform heat generation rate q have been used in the Dirichlet case, while different values of the transfer coefficient h were used in the Robin case. Simulations were then carried out considering the cases of a temperature independent thermal conductivity (as for the analytic solution) and that of a temperature dependent thermal conductivity.

The results of these tests are shown in Figure 8 and Figure 9, respectively. The numerical results for the temperature independent case are seen to overlap the expected analytic solutions. Using a temperature-dependent thermal conductivity in the simulation results in a rise in the temperature distribution of approximately 2% in the case of a Robin condition with $h = 2e5 \frac{W}{m^2}$, 0.08% with $h = 1e7 \frac{W}{m^2}$, 0.8% in the case of a Dirichlet condition with $q = 5.34e16 \frac{W}{m^3}$, and 0.0006 % with $q = 5.34e13 \frac{W}{m^3}$. This rise in temperature is expected due to a decrease in thermal conductivity as the temperature increases. The difference between the constant and temperature dependent-thermal conductivity temperature distributions also increases as the temperatures become higher, e.g., a roughly 2% difference for the Robin condition with $h = 2e5 \frac{W}{m^2}$ with $h = 2e5 \frac{W}{m^2}$ where the peak temperature for the constant case is 350.75K but only a 0.08% change with $h = 1e7 \frac{W}{m^2}$ where the peak temperature is 301.27K. Due to the weak non-linearity in the k vs T relationships, the accuracy of the simulated result in the constant k case, and the behavior of the changes in the temperature distributions of the dependent k simulations we conclude that the use of our Kirchhoff transformation approach is justified.

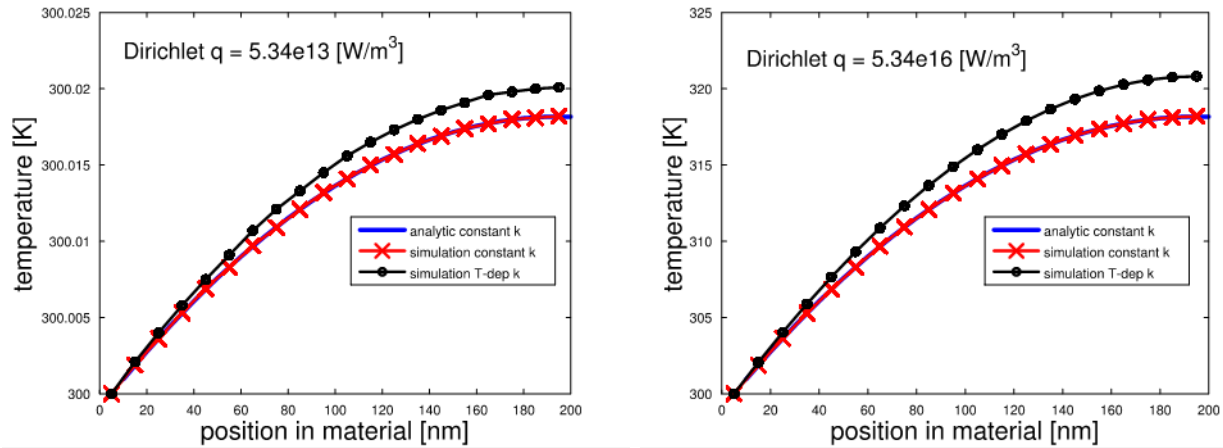


Figure 8: Results for the Dirichlet Boundary Condition

The constant thermal conductivity simulation (red) is seen to overlap the analytic solution (blue), while the simulation with a temperature-dependent thermal conductivity reaches higher peak temperatures as expected due the inverse relationship between thermal conductivity and temperature

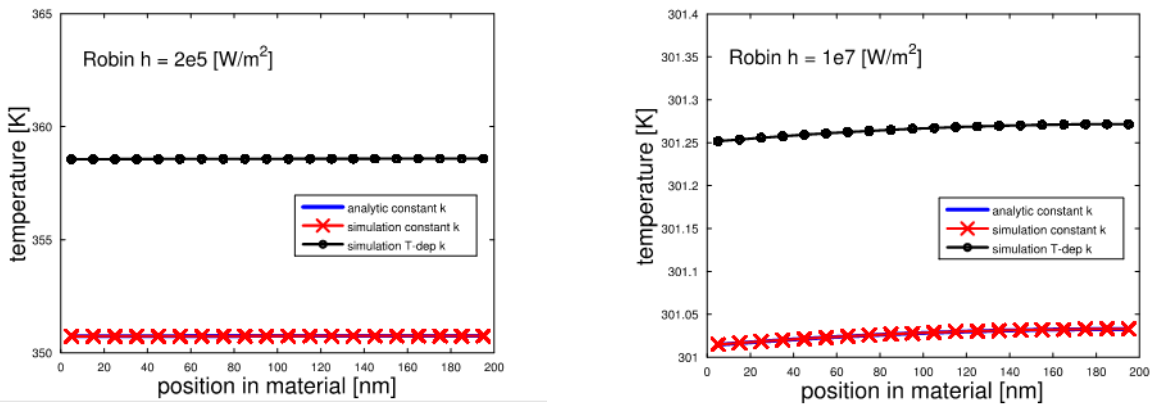


Figure 9: Results for the Robin Boundary Condition

The constant thermal conductivity simulation (red) overlaps the analytic solution (blue), while the simulation using a temperature-dependent thermal conductivity reaches higher peak temperatures due to the inverse relationship between thermal conductivity and temperature

5.0 Conclusions

This project presented a novel modeling approach for the development of a technology based on the microscopic thermal management of solid-state devices. New techniques that model the phonon dynamics within a full spectrum framework have been presented along the comparison between simulated and experimental results. A rejection technique has been implemented to adapt the electron scattering rates to the local conditions, and the thermal conductivity has been correctly reproduced using phonon-phonon and isotope scattering within a particle based approach.

In addition, an energy balance approach derived from the phonon BTE was successfully manipulated into the form of an elliptic PDE through the implementation of the Kirchhoff Transformation, and agreement with analytical solutions was demonstrated. Boundary conditions relevant to thermal simulations were also explored resulting in the implementation of the Robin boundary condition.

6.0 References

- [1] M. Saraniti and S. Goodnick, "Hybrid Fullband Cellular Automaton/Monte Carlo Approach for Fast Simulation of Charge Transport in Semiconductors," *IEEE Transactions on Electron Devices*, vol. 10, no. 47, p. 1909–1915, 2000.
- [2] P. Klemens, "Anharmonic Decay of Optical Phonons," *Phys. Rev.*, no. 148, p. 845, 1966.
- [3] G. P. Srivastava, *The Physics of Phonons*, New York, NY: CRC Press, 1990.
- [4] K. Fuchs, "The conductivity of thin metallic films according to the electron theory of metals," *Proc. Cambridge Philos. Soc.* 34, 100, vol. 34, no. 1, pp. 100-1008, 1938.
- [5] E. H. Sondheimer, "The mean free path of electrons in metals," *Adv. Phys.*, vol. 1, no. 1, p. 1, 1952.
- [6] T. Gonzales. and D. Pardo, " Physical models of ohmic contacts for Monte Carlo device simulation," *Solid-State Electronics*, vol. 39, no. 4, pp. 555-562, 1996.
- [7] M. G. Holland, "Phonon Scattering in Semiconductors from Thermal Conductivity Studies," *Phys. Rev* , vol. 134, pp. A471 - A480, 1964.
- [8] A. V. Inyushkin et al, "On the Isotope Effect in Thermal Conductivity of Silicon," *Phys. Stat. Sol*, vol. 1, no. 11, pp. 2995-2998, 2004.
- [9] T. Ruf et al, "Erratum to Thermal Conductivity of Isotopically Enriched Silicon," *Solid State Communications*, vol. 127, p. 257, 2003.
- [10] M. G. Burzo, P.L. Komarov, and P.E. Raad, "Non-Contact Thermal Conductivity Measurements of Gold Covered Natural and Isotopically-Pure Silicon and Their Respective Oxides," in *5th International Conference on Thermal, Mechanical, and Thermo-mechanical Simulation and Experiments in Micro-Electronics and Micro-systems*, Brussels, Belgium, 2004.
- [11] Capinski et al, "Thermal Conductivity of Isotopically Enriched Si," *Appl. Phys. Letters*, vol. 71, p. 2109, 1997.
- [12] T. Ruf, "Thermal Conductivity of Isotopically Enriched Silicon," *Solid State Comm*, vol. 115, pp. 243-247, 2000.
- [13] V. Palankovski and S. Selberherr, "Thermal Models for Semiconductor Device Simulation," in *IEEE Proc. European Conference on High Temperature Electronics*, Berlin, Germany, 1999.
- [14] K. Fushinobu, A. Majumdar, and K. Hijikata, "Heat Generation and Transport in Submicron Semiconductor Devices," *Journal of Heat Transfer*, vol. 117, pp. 25-31, 1995.
- [15] J. W. Thomas, *Numerical Partial Differential Equations: Conservation Laws and Elliptic Equations*, New York, NY: Springer-Verlag, 1999.
- [16] D. Bleekder and G. Csordas, *Basic Partial Differential Equations*, Cambridge, MA: International Press, 2003.
- [17] Synopsys Version H-2013.03, Mountain View, CA: Synopsys, Inc., 2013.
- [18] MATLAB R2013a, Natick, Massachusetts: The Mathworks, Inc., 2013.

LIST OF SYMBOLS, ABBREVIATIONS, AND ACRONYMS

ACRONYM	DESCRIPTION
BTE	Boltzmann Transport Equation
CAD	computer-aided design
CMC	Cellular Monte Carlo
EMC	Ensemble Monte Carlo
GaAs	gallium arsenide
HTE	Heat Transport Equation
DARPA	Defense Advanced Research Projects Agency
K	kelvin
MAA	months after award
PDE	partial differential equation
Si	silicon
Tloc	local temperature
Tmax	maximum temperature
USAF	United States Air Force